MOX-Report No. 103/2024

A comparative analysis of mesh-based and particle-based numerical methods for landslide run-out simulations

Fois, M.; Gatti, F.; de Falco, C.; Formaggia, L.

MOX, Dipartimento di Matematica
Politecnico di Milano, Via Bonardi 9 - 20133 Milano (Italy)

mox-dmat@polimi.it https://mox.polimi.it

A comparative analysis of mesh-based and particle-based numerical methods for landslide run-out simulations

Marco Fois [(1)] Federico Gatti [(2)] Carlo de Falco[(1)] Luca Formaggia[(1)]

December 3, 2024

[(1)] MOX – Modelling and Scientific Computing
Dipartimento di Matematica, Politecnico di Milano
Piazza Leonardo da Vinci, 20133 Milano, Italy
marco.fois@polimi.it
carlo.defalco@polimi.it
luca.formaggia@polimi.it
[(2)] Seminar for Applied Mathematics (SAM),
Department of Mathematics, ETH Zürich,
CH-8092 Zürich, Switzerland
federico.gatti@math.ethz.ch

Keywords: Semi-conservative Depth Averaged MPM, Path-conservative methods, Implicit-explicit Runge-Kutta-Chebychev scheme, Depth-averaged models, Geohazard analysis.

AMS Subject Classification: 35Q35, 35L65, 35Q70, 65Z05, 76D05, 76D99

Abstract

Landslides are among the most dangerous natural disasters, with their unpredictability and potential for catastrophic human and economic losses exacerbated by climate change. Continuous monitoring and precise modeling of landslide-prone areas are crucial for effective risk management and mitigation. This study explores two distinct numerical simulation approaches: the mesh-based finite element model and the particle-based model. Both methods are analyzed for their ability to simulate landslide dynamics, focusing on their respective advantages in handling complex terrain, material interactions, and large deformations. A modified version of the second-order Taylor-Galerkin scheme and the depth-averaged Material Point Method are employed to model gravity-driven free surface flows, based on depth-integrated incompressible Navier-Stokes equations. The methods are rigorously tested against benchmarks and applied to a real-world scenario to assess their performance, strengths, and limitations. The results offer insights into selecting appropriate simulation techniques for landslide analysis, depending on specific modeling requirements and computational resources.

1 Introduction and motivations

Given their intrinsic unpredictability and potential for catastrophic human and economic losses, landslides are among the most dangerous types of natural disasters exacerbated by climate change [1, 2]. Continuous monitoring of landslide-prone areas is essential. Although in-situ detection techniques, such as strain gauges and piezometers, enable accurate monitoring of surface displacement and internal pressure, satellite surveys provide comprehensive topography and elevation data for the research region [3]. However, empirical monitoring alone is frequently insufficient for managing hazardous situations, including prevention [4, 5]. The high expense and technical complexity of realistic experimental assessments underscore the need for precise numerical simulation models for landslides.

Landslides exhibit multifaceted phenomenology that occurs in multiple stages. In the initial stage, landslides can be thought of as rigid structures affected by hydrodynamic soil conditions, pore

pressure, and gravity, leading to sporadic slides and sudden changes in velocity. Conversely, the progression and evolution of the landslide front during the run-out phase depend on local rheology and topography, which are primarily controlled by advection and involve viscoplastic behavior. With sustained horizontal velocities [6], the run-out phase behaves like a fluid in situations such as debris flows or mudslides. The goal of this effort is to track the advancing front and simulate the evolution of rapidly moving landslides immediately upon their initiation. This is a crucial step in forecasting affected areas and calculating or preventing damage.

In the context of numerical simulations of landslide scenarios, mesh-based finite element models and particle-based models represent two distinct approaches, each with specific advantages and limitations [7, 8]. Mesh-based finite element models divide the domain into discrete elements and solve differential equations locally on each element. They offer good adherence to terrain geometry and material interfaces, making them suitable for modeling both solid and fluid behaviors. However, they are computationally intensive, especially for complex geometries and fine meshes, and may struggle with fracture propagation and discontinuities. In contrast, particle-based models represent materials through discrete particles that carry physical properties. They are adaptable to large deformations and fracture phenomena and handle solid-fluid interactions effectively. This makes them efficient for simulations involving significant deformations and fractures, particularly in scenarios with complex flow patterns [9, 10]. However, they can become more computationally demanding with increasing particle counts compared to the finite element approach. The choice between these methods depends on the specific scenario and simulation goals. Large deformations and solid-fluid interactions may be better handled by particle-based methods in large-scale occurrences, such as landslides over extensive terrains. Finite element approaches, however, might be preferred for simulations requiring precise structural modeling or accurate depiction of material interactions. A comparative analysis helps in choosing the best strategy based on the specific needs of the problem and the available computational resources.

To this end, we select two numerical methods: a modified version of the second-order Taylor-Galerkin (TG2), and the Depth-averaged MPM (DAMPM). Regarding the TG2 scheme, we consider a modified version of the classical implementation that achieves well-balancing and the ability to handle stiff reaction-diffusion operators, which is the Path-conservative Implicit-Explicit TG2 (IMEX-TG2-PC). This modified TG2 has been described in a series of works [6, 11, 12, 13]. For the DAMPM, we particularly rely on the implementation described in [14]. Both methods were applied to the same set of equations to describe gravity-driven free surface flows, derived from the depth-integrated incompressible Navier-Stokes equation, and were rigorously tested against benchmarks. Finally, we assess their performance in a real-world scenario, analyzing strengths and limitations. The paper is organized as follows. Section 2 presents the physical model, including the constitutive and rheological laws. Section 3 discusses the numerical framework adopted, analyzing both methods and discretizing the differential problem. In Section 4, we show some numerical results, including reliability and well-balancing tests. At the end of Section 4, a real test case is presented, and some conclusions and perspectives are presented in Section 5.

2 Governing equations

Depth-averaged models are one of the better solutions for modeling the dynamics of mudflows and landslides because they make flow on sloping terrain with shallow depths easier to portray. These models are valid approximations for free-surface flows over gently sloping terrains with fluid depths substantially smaller than the horizontal length scale of the terrain, based on the conservation equations of mass and momentum. The following are important presumptions under which these models can be used:

(i) hydrostatic pressure predominates over dynamic pressure in a flow that is extensively controlled by gravity.

(ii) Since the fluid depth is assumed to be much smaller than the horizontal extent of the terrain, flow equations can be simplified and motion is treated as primarily two-dimensional.

(iii) The terrain features moderately inclined slopes where the vertical component of velocity is negligible compared to the horizontal component, and negligible three-dimensional effects are present, such as vertical currents, which may be trifling in situations where fluid depth is small relative to the horizontal extent of the terrain.

Under these assumptions, depth-integrated models offer an accurate portrayal of fluid-like flow dynamics on complex terrains, encompassing erosion, sediment transport, and deposition phenomena pivotal in landslide and mudflow simulations.

Let $\Omega \subset \mathbb{R}^2$ be a Cartesian domain and let $(0, T]$ be a time interval with $T > 0$. On $\Omega_w \subset \Omega$ defined as the region where the material height $h > 0$, we consider the following set of depth-averaged balance equations derived from the Saint Venant equations [15, 16, 17, 18] for h and linear momenta hu, hv

$$\begin{cases} \partial_t h + \partial_x(hu) + \partial_y(hv) = 0, \\ \partial_t(hu) + \partial_x\left(hu^2 + \frac{1}{2}gh^2\right) + \partial_y(huv) = \frac{1}{\rho}\partial_x(h\sigma_{xx}) + \frac{1}{\rho}\partial_y(h\sigma_{xy}) + \frac{1}{\rho}B_x^f - gh\partial_x Z, \\ \partial_t(hv) + \partial_x(hvu) + \partial_y\left(hv^2 + \frac{1}{2}gh^2\right) = \frac{1}{\rho}\partial_x(h\sigma_{xy}) + \frac{1}{\rho}\partial_y(h\sigma_{yy}) + \frac{1}{\rho}B_y^f - gh\partial_y Z, \end{cases} \tag{1}$$

where $\mathbf{v} := [u, v]^T$ is the horizontal velocity vector, g the gravitational acceleration, ρ the constant density of the material, $\mathbf{B}^f := [B_x^f, B_y^f]^T$ the bed friction, $Z = Z(x, y)$ the orography profile and $\boldsymbol{\sigma} := [\sigma_{xx}, \sigma_{yy}, \sigma_{xy}]$ the deviatoric part of the Cauchy stress tensor.

2.1 Rheological and constitutive model

The combination of a turbulent and a frictional model is justified by the nature of the phenomena under investigation, and it has been demonstrated that this assumption yields favorable results for velocity and deposition in simulations [19, 20, 21]. For this purpose, we have considered in the right-hand-side of equation (1) a bed friction $\mathbf{B}^f$ described by the Voellmy model and defined by

$$\mathbf{B}^f = -\left(\rho g h \tan\varphi \ \mathrm{sgn}\mathbf{v} + \frac{\rho g|\mathbf{v}|^2}{\xi}\right)\frac{\mathbf{v}}{|\mathbf{v}|}, \tag{2}$$

where φ represents the friction angle, sgn the the signum function and ξ the turbulence coefficient. Regarding the constitutive law, we adopted a depth-integrated variant of the Bingham rheological model for visco-plastic materials, by defining the Cauchy stress tensor $\boldsymbol{\sigma}$ as

$$\boldsymbol{\sigma} = \left(2\mu + \frac{\tau_Y}{\mathcal{I}_2}\right)\mathbf{D}. \tag{3}$$

where μ is the material viscosity, τ_Y the yield shear stress, $\mathbf{D}$ represents the strain rate tensor defined by

$$\mathbf{D} = \begin{bmatrix} \partial_x u & \frac{1}{2}(\partial_y u + \partial_x v) \\ \frac{1}{2}(\partial_x u + \partial_y v) & \partial_y v \end{bmatrix}, \tag{4}$$

and $\mathcal{I}_2 := \frac{1}{2}\bar{\mathbf{D}} : \bar{\mathbf{D}}$ is the second invariant of the depth-averaged strain rate tensor

$$\bar{\mathbf{D}} = \begin{bmatrix} D_{11} & D_{12} & \frac{1}{2}\partial_z u \\ D_{21} & D_{22} & \frac{1}{2}\partial_z v \\ \frac{1}{2}\partial_z u & \frac{1}{2}\partial_z v & -(D_{11} + D_{22}) \end{bmatrix}. \tag{5}$$

Here we used the hyphotesis of incompressibility constraint to set $\bar{D}_{33} = -(D_{11} + D_{22})$.

In order to compute the second invariant $\mathcal{I}_2$ we need to estimate $\partial_z u$ and $\partial_z v$. Under the assumptions of steady-state, laminar, and simple shear fluid, the vertical derivative of the velocity field can be estimate as

$$\partial_z \mathbf{v} = \frac{3}{2 + \psi}\frac{\mathbf{v}}{h}, \tag{6}$$

where $\psi = \tau_Y/\tau_B \in [0,1]$ and τ_B is the bed resistance force. To compute the quantity ψ, we resort to the optimal second-degree approximation, which provides a maximum error equal to $1/32$, by taking the positive solution of the equation

$$48\psi^2 - (114 + 32a)\psi + 65 = 0, \quad \text{with } a = \frac{6\mu|\mathbf{v}|}{\tau_Y h}. \tag{7}$$

Finally, the invariant $\mathcal{I}_2$ can be obtained by replacing the solution of Equation (7) with (6).

3 Numerical Methods

In this section, we describe the two numerical methods used to solve system (1). We first review the improved version of the TG2 scheme, the split IMEX-TG2-PC, developed in [6, 11, 12, 13]. This enhanced scheme modifies the classical TG2 method by achieving the well-balancing property and overcoming the stiffness of diffusion-reaction terms while maintaining strong scaling performances characteristics of the original TG2 implementation. In particular, this modified TG2 scheme is able to separate the time scales. Then, in Section 3.2, we describe the particle-based method employed in this study, which has been extensively detailed in [14, 22, 23] and which is a semi-conservative variant of the Depth-averaged Material Point Method (DAMPM).

3.1 The TG2-PC scheme

Before proceeding with the description of the method, it is appropriate to provide a more compact formulation of the model equations. This will simplify the presentation and facilitate the discussion of the numerical approach.

We consider a rectangular domain $\Omega \subset \mathbb{R}^2$ with a subdomain $\Omega_w \subset \Omega$, representing the time-dependent region where the landslide material depth $h > 0$. The system shown in (1) can be expressed in a more general and compact way as

$$\partial_t \mathbf{q} + \nabla \cdot \mathbf{F} + \nabla \cdot \mathbf{G} + \mathbf{B}\nabla Z = \mathbf{r} \quad \text{in} \quad \Omega_w \times (0, T], \tag{8}$$

The system is equipped with appropriate boundary and initial conditions, where $\mathbf{q} \in \mathbb{R}^4$ is the vector of conserved variables, $\mathbf{F} \in \mathbb{R}^{4\times 2}$ the transport flux tensor, $\mathbf{G} \in \mathbb{R}^{4\times 2}$ the diffusive flux tensor, $\mathbf{B} \in \mathbb{R}^{4\times 2}$ the matrix of non-conservative terms, Z the orography profile, $\mathbf{r} \in \mathbb{R}^4$ the reaction term, and $(0, T]$ the time window of interest.

Here, $\mathbf{q} = [h, U_x, U_y, Z]^T$, with $U_x = hu$ and $U_y = hv$ as the mass fluxes in the x- and y-directions, respectively.

The transport flux tensor is:

$$\mathbf{F}(\mathbf{q}) = \begin{bmatrix} U_x & U_y \\ \frac{U_x^2}{h} + \frac{1}{2}gh^2 & \frac{U_y U_x}{h} \\ \frac{U_y U_x}{h} & \frac{U_y^2}{h} + \frac{1}{2}gh^2 \\ 0 & 0 \end{bmatrix},$$

where g is the gravitational constant.

The diffusive flux tensor is:

$$\mathbf{G}(\mathbf{q}, \nabla\mathbf{q}) = \begin{bmatrix} 0 & 0 \\ -\frac{1}{\rho}\sigma_{xx}h & -\frac{1}{\rho}\sigma_{xy}h \\ -\frac{1}{\rho}\sigma_{xy}h & -\frac{1}{\rho}\sigma_{yy}h \\ 0 & 0 \end{bmatrix},$$

where ρ is the material density (assumed constant), and $\{\sigma_{ij}\}_{i,j=x,y}$ are the components of the deviatoric Cauchy stress tensor $\boldsymbol{\sigma}$.

The non-conservative matrix is:

$$\mathbf{B}(\mathbf{q}) = \begin{bmatrix} 0 & 0 \\ gh & 0 \\ 0 & gh \\ 0 & 0 \end{bmatrix}.$$

The reaction term is:

$$\mathbf{r}(\mathbf{q}) = \begin{bmatrix} 0 \\ \frac{1}{\rho} B_x^f \\ \frac{1}{\rho} B_y^f \\ 0 \end{bmatrix},$$

where $B_i^f(\mathbf{q})$, $i = x, y$, represents the bed friction described in (2) .

The two-step Taylor-Galerkin (TG2) method relies on a Taylor series expansion in time, which, as highlighted in [24], provides an effective alternative to Runge-Kutta time integration for non-stiff problems. One notable advantage of the TG2 scheme is that it requires applying the flux limiting procedure only once per time step, whereas Runge-Kutta methods necessitate this correction at every stage of the process.

In this work, we introduce a novel modification to the conventional explicit TG2 scheme by incorporating non-conservative contributions using a predictor-corrector (PC) approach. For an overview of the explicit TG2 scheme applied to fast landslide simulations, we refer the reader to [25, 6].

Let us now consider a hyperbolic problem with non-conservative terms, corresponding to model (8) where the diffusive fluxes $\mathbf{G}$ and the source term $\mathbf{r}$ are neglected. This simplification is equivalent to frictionless shallow-water equations over a fixed bottom topography (i.e., $\partial_t Z = 0$).

At a generic time level t^{n+o}, where $o = 0, \frac{1}{2}, 1$, we denote by $\mathbf{Q}^{n+o} \approx \mathbf{q}^{n+o}$ the discrete approximation of the conservative variable at t^{n+o}. Let $\mathbf{F}^{n+o} = \mathbf{F}(\mathbf{Q}^{n+o})$ and $\mathbf{B}^{n+o} = \mathbf{B}(\mathbf{Q}^{n+o})$. The following two-step, second-order semi-discrete scheme is employed for time integration of system (8) between the time levels t^n and t^{n+1}:

$$\begin{cases} \mathbf{Q}^{n+\frac{1}{2}} = \mathbf{Q}^n + \dfrac{\Delta t}{2} \left(-\nabla \cdot \mathbf{F}^n - \mathbf{B}^n \nabla Z^n\right), \\ \mathbf{Q}^{n+1} = \mathbf{Q}^n + \Delta t \left[-\nabla \cdot \mathbf{F}^{n+\frac{1}{2}} - \mathbf{B}^{n+\frac{1}{2}} \nabla Z^{n+\frac{1}{2}}\right], \end{cases} \tag{9}$$

where the first equation coincides with a first-order predictor step used to approximate the conservative variables at the intermediate time.

Next, we consider the spatial discretization using the finite element method to derive the fully discrete scheme. The domain Ω is divided into a family $\{\mathcal{D}_h\}$ of structured quadrilateral meshes with a characteristic spacing h. For the discretization, we define two finite-dimensional spaces associated with $\mathcal{D}_h$: the space $\mathbb{Q}_0$, consisting of (discontinuous) piecewise constant polynomials, is used for the first step in (9), while the space $\mathbb{Q}_1$, composed of continuous piecewise bilinear polynomials, is used for the second step.

Specifically, the intermediate variable $\mathbf{Q}^{n+\frac{1}{2}}$ is approximated in the space $\mathbb{Q}_0$, whereas the variables $\mathbf{Q}^n$ and $\mathbf{Q}^{n+1}$ are chosen in $\mathbb{Q}_1$. The basis functions for the spaces $\mathbb{Q}_0$ and $\mathbb{Q}_1$ are denoted by $\{\phi_j^{(0)}, j = 1, \ldots, M\}$ and $\{\phi_i^{(1)}, i = 1, \ldots, N\}$, respectively, where M is the number of quadrilateral elements in $\mathcal{D}_h$, and N is the total number of mesh nodes. The resulting fully discrete weak formulation

can be expressed as:

$$(\mathbf{Q}^{n+\frac{1}{2}}, \phi_j^{(0)}) = (\mathbf{Q}^n, \phi_j^{(0)}) - \frac{\Delta t}{2}(\nabla \cdot \mathbf{F}^n, \phi_j^{(0)}) - \frac{\Delta t}{2}(\mathbf{B}^n \nabla Z^n, \phi_j^{(0)}),$$
$$(\mathbf{Q}^{n+1}, \phi_i^{(1)}) = (\mathbf{Q}^n, \phi_i^{(1)}) + \Delta t\,(\mathbf{F}^{*,n+\frac{1}{2}}, \nabla \phi_i^{(1)}) - \Delta t\,(\mathbf{B}^{n+\frac{1}{2}} \nabla Z^{n+\frac{1}{2}}, \phi_i^{(1)}), \tag{10}$$

for $j = 1, \ldots, M$, $i = 1, \ldots, N$, where $(\cdot, \cdot)$ indicates the $L^2(\Omega)$-scalar product, while $\mathbf{F}^{*,n+\frac{1}{2}}$ is a discretization flux that we define below.

In this fully discrete weak formulation, we have omitted the boundary integrals over the computational domain boundary $\partial\Omega$, specifically the term $\int_{\partial\Omega} \mathbf{F}^{*,n+\frac{1}{2}}\,\mathbf{n}\,\phi_i^{(1)}\,d\Sigma$, where $\mathbf{n}$ represents the outward unit normal vector to $\partial\Omega$. Boundary conditions are imposed on this boundary. A comprehensive analysis of boundary conditions for hyperbolic problems lies beyond the scope of this work. Here, we employ non-reflecting boundary conditions; for further details, the reader is referred to [26].

Following the approach in [27], we apply the mass lumping technique in the second step of Equation (10) to avoid inverting the consistent mass matrix. This choice is particularly advantageous for parallel computation, as it allows each computation in the second step to be performed independently at each node.

Furthermore, we emphasize two key challenges in the computation of this step: the evaluation of the integral of the non-conservative product and the development of a high-order flux discretization that ensures both the well-balancing and positivity-preserving properties. Let us focus on the former issue.

We build upon the path-conservative (PC) framework, which offers a rigorous analytical interpretation of non-conservative products in a weak sense [28]. Utilizing a PC approach enables the modification of the scheme to guarantee the well-balancing property by appropriately choosing a path.

Although the PC strategy has been extensively used in discrete formulations, such as finite volume methods [29, 30] and discontinuous Galerkin (DG) schemes [31], to the best of the authors' knowledge, it has not yet been applied within a continuous finite element framework, nor specifically within the context of the TG2 scheme.

The PC approach provides an analytical interpretation of the non-conservative products evaluated during the intermediate step in the second stage of the method, ensuring the well-balancing property for the system of equations under consideration. However, it is important to note that the PC method is not without limitations. As discussed in [32], the PC framework may not always replicate the solution expected from a conservative numerical solver.

We now proceed to define a path that ensures the desired properties.

$$\mathbf{\Psi} = \mathbf{\Psi}(\mathbf{Q}_-^{n+\frac{1}{2}}, \mathbf{Q}_+^{n+\frac{1}{2}}, s) = \mathbf{Q}_-^{n+\frac{1}{2}} + s(\mathbf{Q}_+^{n+\frac{1}{2}} - \mathbf{Q}_-^{n+\frac{1}{2}}), \tag{11}$$

which connects two orography states, $\mathbf{Q}_-^{n+\frac{1}{2}}$ and $\mathbf{Q}_+^{n+\frac{1}{2}}$, related to two mesh elements sharing the same edge e, with s the parameter spanning the path, for $0 \leq s \leq 1$. We choose a standard linear path.

As discussed in [33], the motivation for the specific choice of the path lies in its simplicity, as well as its ability to ensure that the resulting scheme is exactly well-balanced for the so-called lake-at-rest solutions of shallow-water-type equations.

Let us denote by $\mathcal{E}_i$ the set of edges e connected to the node i. The path-conservative (PC) nodal formulation for the non-conservative product in the second step (10) becomes

$$(\mathbf{B}^{n+\frac{1}{2}} \nabla Z^{n+\frac{1}{2}}, \phi_i^{(1)}) = \sum_{e \in \mathcal{E}_i} \int_e \phi_i^{(1)} dl \int_0^1 \mathbf{B}\big(\mathbf{\Psi}(\mathbf{Q}_-^{n+\frac{1}{2}}, \mathbf{Q}_+^{n+\frac{1}{2}}, s)\big)\mathbf{n}_e\,\partial_s \mathbf{\Psi} ds, \tag{12}$$

where $\mathbf{n}_e$ is the unit normal to the edge, such that $\mathbf{n}_e \cdot (\mathbf{x}_+ - \mathbf{x}_-) > 0$ with $\mathbf{x}_+$ and $\mathbf{x}_-$ the coordinates of the barycenter of two elements sharing edge e, while $\partial_s \mathbf{\Psi}$ denotes the derivative along the selected path. Finally, the two integrals are numerically computed with the trapezoidal quadrature rule. The well-balancing property is ensured by the proposition proved in [11] and which is given by

Proposition 3.1. *The fully discrete weak-form* (10) *with the non-conservative contribution in* (12) *is exact in the modeling of the lake-at-rest condition at the discrete level.*

We now turn to the development of a high-order discretization flux $\mathbf{F}^{*,n+\frac{1}{2}}$. Since the TG2 scheme, being second-order accurate in both space and time [34], is neither monotone nor positivity-preserving, we employ Zalesak multidimensional Flux Corrected Transport (FCT) method [35, 36, 37] to suppress spurious oscillations near discontinuities (e.g., the Gibbs phenomenon) and ensure a positivity-preserving, oscillation-free physical solution.

To formalize the well-balanced FCT method used, consider a single quadrilateral element Q of the discretized domain, with resolution $\Delta x \times \Delta y$, and define the variable $\tilde{\mathbf{v}} = \mathbf{U}\mathbf{q}$. As noted in [6], the procedure relies on the Rusanov first-order monotone flux, adjusted by a flux-limiting correction coefficient to achieve the desired properties.

However, it is important to note that the FCT strategy does not inherently preserve the well-balanced property of the numerical scheme. This limitation, common to many flux limiters, has already been addressed in the context of discontinuous Galerkin (DG) methods [38]. Below, we describe a similar procedure tailored to the approximation of shallow water equations, inspired by the DG approach presented in that work.

To formalize the adopted well-balanced FCT method, let us consider a single quadrilateral element, Q, of the domain discretization with resolution $\Delta x \times \Delta y$ and consider the variable $\tilde{\mathbf{v}} = \mathbf{U}\mathbf{q}$, with

$$\mathbf{U} = \begin{bmatrix} 1 & 0 & 0 & u \\ 0 & 1 & 0 & 0 \\ 0 & 0 & 1 & 0 \\ 0 & 0 & 0 & 0 \end{bmatrix} \tag{13}$$

and $u = u(H - H_{\min})$ the Heaviside step function. Then, the Rusanov anti-diffusive flux is defined as,

$$\delta\mathbf{F}_Q^n = \min_{(\frac{\Delta x}{\Delta t}, \frac{\Delta y}{\Delta t})} \frac{1}{2\Delta t}(\nabla\tilde{\mathbf{V}}^n, \phi_Q^{(0)}), \tag{14}$$

with $\phi_Q^{(0)}$ the $\mathbb{Q}_0$-basis function associated with element Q and $\tilde{\mathbf{V}}^n$ the time discrete counter-part of the variable $\tilde{\mathbf{v}}$, i.e., $\tilde{\mathbf{V}}^n = \mathbf{U}^n\mathbf{Q}^n$.

The exact integration in (14) produces an anti-diffusive flux, expressed as a linear function of the ratios $\frac{\Delta x}{\Delta t}$ and $\frac{\Delta y}{\Delta t}$. Due to the Courant–Friedrichs–Lewy (CFL) condition, these ratios are lower bounded by the maximum absolute value of the simple wave speeds within the element Q along the x- and y-directions. The simple waves correspond to the eigenvalues of the full semi-linear system, which incorporates both conservative and non-conservative contributions.

The discrete flux within the element Q is then expressed as:

$$\mathbf{F}_Q^{*,n+\frac{1}{2}} = (\mathbf{F}_Q^{n+\frac{1}{2}} - \delta\mathbf{F}_Q^n) + \alpha_Q\delta\mathbf{F}_Q^n, \tag{15}$$

where $\alpha_Q \in \mathbb{Q}_0$ is the piecewise constant FCT coefficient, determined following the Zalesak procedure [35, 36, 37] (for details on the implementation, see [6]).

It is important to note that the Zalesak procedure ensures a positivity-preserving approximation only if the underlying low-order scheme itself is positivity-preserving. For the specific low-order discretization flux considered here, the following result, proved in [11], holds:

Proposition 3.2. *The low-order TG2-PC scheme yields a positivity-preserving discretization for the free-surface height.*

3.1.1 The second order IMEX-RKC finite element scheme

To address the stiffness of the diffusion and source terms, we employ a second-order space-time Implicit-Explicit Runge-Kutta-Chebychev (IMEX-RKC) finite element scheme. This method avoids the computational cost of constructing a global matrix, as required by fully implicit schemes, while retaining a node-wise operation structure well-suited for parallel implementation.

Focusing on the diffusion-reaction equation, we neglect the hyperbolic contributions from $\mathbf{F}$ and $\mathbf{B}$ in model (8). The spatial discretization is performed using the finite element space $\mathbb{Q}_1$ associated with the structured quadrilateral mesh $\mathcal{D}_h$ over Ω. Consequently, at each node i (for $i = 1, \ldots, N$), we solve the resulting semi-discrete problem given by

$$\begin{cases} \frac{d}{dt}\tilde{\mathbf{V}}_i = \mathbf{F_D}(t, \tilde{\mathbf{V}}_{\mathcal{N}_i}) + \mathbf{F_R}(t, \tilde{\mathbf{V}}_i), \\ \mathbf{F_D}(t, \tilde{\mathbf{V}}_{\mathcal{N}_i}) = (\mathbf{G}, \nabla\phi_i^{(1)}), \\ \mathbf{F_R}(t, \tilde{\mathbf{V}}_i) = (\mathbf{r}, \phi_i^{(1)}). \end{cases} \tag{16}$$

Here, $\tilde{\mathbf{V}}_i = (\mathbf{q}, \phi_i^{(1)})$ represents a vector of time-dependent functions, discretizing the conserved variable $\mathbf{q}$ at node i, with the integral computed using a mass lumping approach. The terms $\mathbf{F_D}(t, \tilde{\mathbf{V}}_{\mathcal{N}_i})$ and $\mathbf{F_R}(t, \tilde{\mathbf{V}}_i)$ represent the spatial discretizations of the diffusive fluxes and the reaction term, respectively. The symbol $\tilde{\mathbf{V}}_{\mathcal{N}_i}$ denotes the discretization of $\mathbf{q}$ at the nodes within the patch of elements associated with node i.

In this semi-discrete formulation, we omit boundary conditions on the diffusive fluxes by assuming $\int_{\partial\Omega} \mathbf{G}\,\mathbf{n}\,\phi_i^{(1)}\, d\Sigma = \mathbf{0}$. A detailed treatment of boundary conditions for purely diffusive problems lies outside the scope of this work. For simplicity, we consider null boundary fluxes, noting that in advection-dominated problems, transport fluxes typically have the most significant impact.

It is well-established that when using linear finite elements for the spatial discretization of diffusive fluxes, the resulting space-discrete operator has eigenvalues that lie on the real axis and are all negative, as noted in [39, 40].

To address this, we employ the IMEX-RKC time integration scheme [41], which is an extension of the RKC scheme specifically designed for time integration in diffusion problems [39]. This method has already been applied with linear finite elements in [42].

The second-order IMEX-RKC scheme can be formulated as follows: given the numerical solution $\tilde{\mathbf{V}}_i^n$ at time t^n, the updated solution, $\tilde{\mathbf{V}}_i^{n+1}$, is computed by:

$$\begin{cases} \mathbf{W}_i^0 &= \mathbf{V}_i^n, \\ \mathbf{W}_i^1 &- \tilde{\mu}_1 \Delta t\, \mathbf{F}_\mathbf{R}^1(\mathbf{W}_i^1) = \mathbf{W}_i^0 + \tilde{\mu}_1 \Delta t\, \mathbf{F}_\mathbf{D}^0(\mathbf{W}_{\mathcal{N}_i}^0), \\ \mathbf{W}_i^j &- \tilde{\mu}_1 \Delta t\, \mathbf{F}_\mathbf{R}^j(\mathbf{W}_i^j) = (1-\mu_j-\nu_j)\mathbf{W}_i^0 + \mu_j \mathbf{W}_i^{j-1} + \nu_j \mathbf{W}_i^{j-2} \\ &+ \tilde{\mu}_j \Delta t\, \mathbf{F}_\mathbf{D}^{j-1}(\mathbf{W}_{\mathcal{N}_i}^{j-1}) + \tilde{\gamma}_j \Delta t\, \mathbf{F}_\mathbf{D}^0(\mathbf{W}_{\mathcal{N}_i}^0) \\ &+ (\tilde{\gamma}_j \tilde{\mu}_1 \mu_j / \tilde{\mu}_j - (1-\mu_j-\nu_j)\tilde{\mu}_1) \Delta t\, \mathbf{F}_\mathbf{R}^0(\mathbf{W}_i^0) \\ &- \nu_j \tilde{\mu}_1 \Delta t\, \mathbf{F}_\mathbf{R}^{j-2}(\mathbf{W}_i^{j-2}), \quad j = 2, \ldots, m, \\ \mathbf{V}_i^{n+1} &= \mathbf{W}_i^m, \end{cases} \tag{17}$$

where $\mathbf{W}_i^0, \ldots, \mathbf{W}_i^m$ are intermediate vectors in the node i, fluxes $\mathbf{F}_\mathbf{D}^j(\mathbf{W}_{\mathcal{N}_i}^j)$, $\mathbf{F}_\mathbf{R}^j(\mathbf{W}_i^j)$ stand for $\mathbf{F_D}(t^n + c_j\Delta t, \mathbf{W}_{\mathcal{N}_i}^j), \mathbf{F_R}(t^n + c_j\Delta t, \mathbf{W}_i^j)$ respectively, with $0 = c_0 < c_1 < \cdots < c_m = 1$. Again, $\mathbf{W}_{\mathcal{N}_i}^j$ denotes the set of vectors $\mathbf{W}_k^j$, for $k = 1, \ldots, N$, defined at the nodes of the elements that share node i, including node i itself.

The number of stages, m, required to stabilize the second-order RKC method depends on the stiffness of the diffusion term.

As derived in [41], we define the number of stages, m, as

$$m = 1 + \left\lceil \left(1 + \frac{\Delta t\, \sigma_J}{0.653}\right)^{\frac{1}{2}} \right\rceil, \tag{18}$$

where σ_J represents the spectral radius of the Jacobian matrix associated with the space-discrete diffusion operator $\mathbf{F_D}$.

In practice, σ_J is estimated using the Gershgorin circle theorem, and the derivatives in the Jacobian matrix are computed via numerical differentiation. It is worth noting that for applications with a very stiff diffusion term, the spectral radius can become extremely large, reducing the efficiency of

the RKC scheme, as it requires a substantial number of internal stages to stabilize. However, formula (18) remains valid when the diffusion operator is only mildly stiff, while the reaction terms are highly stiff, as in the problem considered in this paper.

For the coefficients in (17), we adopt the definitions from [41], which are provided here for completeness. Specifically, we introduce the Chebychev polynomials of the first kind, defined by the recursive relation:

$$T_0(x) = 1, \quad T_1(x) = x, \quad T_j(x) = 2xT_{j-1}(x) - T_{j-2}(x), \tag{19}$$

for $2 \leq j \leq m$ and $x \in \mathbb{R}$, where index j keeps trace of the polynomial degree; the positive real parameter ϵ, known as dumping parameter, that we set to $2/13$ in order to ensure a second order scheme as underlined in [39, 41]; quantities

$$\omega_0 = 1 + \frac{\epsilon}{m^2}, \quad \omega_1 = \frac{T_m^{'}(\omega_0)}{T_m^{''}(\omega_0)}; \quad b_0 = b_1 = b_2, \quad b_j = \frac{T_j^{''}(\omega_0)}{\left[T_j^{'}(\omega_0)\right]^2}.$$

Thus, coefficients $\mu_j, \nu_j, \tilde{\mu}_j, \tilde{\gamma}_j$ and c_j are computed by

$$\mu_j = \tfrac{2b_j\omega_0}{b_{j-1}}, \quad \nu_j = \tfrac{-b_j}{b_{j-2}}, \quad \tilde{\mu}_j = \tfrac{2b_j\omega_1}{b_{j-1}} \quad \text{with} \quad \tilde{\mu}_1 = b_1\omega_1,$$

$$\tilde{\gamma}_j = -(1 - b_{j-1}T_{j-1}(\omega_0))\tilde{\mu}_j, \quad c_j = \tfrac{T_m^{'}(\omega_0)}{T_m^{''}(\omega_0)}\tfrac{T_j^{''}(\omega_0)}{T_j^{'}(\omega_0)} \quad \text{with} \quad c_0 = 0, \; c_1 = \tfrac{c_2}{4\omega_0},$$

with $2 \leq j \leq m$.

The explicit treatment of the diffusion term in (17) results in a nonlinear algebraic system of equations that is spatially decoupled. Consequently, only a single nonlinear equation needs to be solved at each mesh node for every internal stage of the IMEX-RKC method, facilitating a fully decoupled system similar to the TG2 scheme. Since the mass conservation equation does not depend on the diffusion term, the RKC internal stages are performed solely for the momentum equation.

Moreover, the bed friction term included in $\mathbf{F_R}$ depends on the x- and y-mass fluxes separately (as specified by the rheology law in (2)), allowing the nonlinearity at each mesh node to be addressed with a scalar semi-smooth Newton method along both the x- and y-directions without requiring matrix inversion. The semi-smooth Newton method used is similar to those described in [43, 44, 45] for contact problems.

The semi-smooth scheme is chosen because the bed friction term depends on the absolute value of the velocity components, leading to a piecewise differentiable function due to the presence of the signum function. To ensure piecewise differentiability, a linear relaxation of the signum function in (2) is adopted. Specifically, for $x \in \mathbb{R}$, the function $\mathrm{sgn}(x)$ is replaced by the relaxed version

$$\mathrm{sgn}_\gamma(x) = \begin{cases} 1 & \text{if } x > \gamma, \\ -1 & \text{if } x < -\gamma, \\ \dfrac{x}{\gamma} & \text{otherwise,} \end{cases} \tag{20}$$

such that $\mathrm{sgn}(x) = \lim_{\gamma \to 0} \mathrm{sgn}_\gamma(x)$, where γ is a strictly positive relaxation parameter. In the simulations presented here, γ is set to 10^{-2}. Finally, the selected time discretization in the presence of a $\mathbb{Q}_1$ spatial finite element discretization leads to a numerical scheme that is second order in space and time.

3.1.2 Strang splitting IMEX-RKC TG2-PC method

In this section, we present the approximation scheme used for the numerical assessment in the next section. In model (8), the transport and diffusion-reaction terms exhibit distinct numerical characteristics, justifying the use of a splitting method [46, 47] for efficient time integration. Here, we adopt the second-order accurate and strongly stable Strang splitting [46].

For clarity, we define the transport and diffusion-reaction continuous operators as $\mathcal{T}(\mathbf{q}) = -\nabla \cdot \mathbf{F} - \mathbf{B}\nabla Z$ and $\mathcal{D}(\mathbf{q}, \nabla\mathbf{q}) = \mathbf{r} - \nabla \cdot \mathbf{G}$, respectively. The Strang splitting method follows this three-step procedure: given $\mathbf{q}^n$,

$$
\begin{aligned}
&\partial_t \mathbf{q}^{(1)} = \mathcal{T}(\mathbf{q}^{(1)}) \quad \text{with} \quad \mathbf{q}^{(1)}(\mathbf{x}, t^n) = \mathbf{q}^n, \\
&\partial_t \mathbf{q}^{(2)} = \mathcal{D}(\mathbf{q}^{(2)}, \nabla\mathbf{q}^{(2)}) \quad \text{with} \quad \mathbf{q}^{(2)}(\mathbf{x}, t^n) = \mathbf{q}^{(1)}\Big(\mathbf{x}, t^n + \frac{\Delta t}{2}\Big), \\
&\partial_t \mathbf{q}^{(3)} = \mathcal{T}(\mathbf{q}^{(3)}) \quad \text{with} \quad \mathbf{q}^{(3)}\Big(\mathbf{x}, t^n + \frac{\Delta t}{2}\Big) = \mathbf{q}^{(2)}(\mathbf{x}, t^n + \Delta t), \\
&\mathbf{q}^{n+1} = \mathbf{q}^{(3)}(\mathbf{x}, t^n + \Delta t),
\end{aligned}
$$

for $n \geq 0$. The Split IMEX-RKC TG2-PC method integrates the first and third steps with the TG2-PC method, and the second step, involving the stiff reaction-diffusion operator, with the IMEX-RKC scheme. The overall scheme is governed only by the CFL condition of the transport operator, as the IMEX-RKC scheme is unconditionally stable. The CFL condition is limited to 2, since the first and third steps use a time step of $\Delta t/2$. Unlike the TG2 method [25, 17, 48, 6], this approach avoids stricter time step restrictions from the reaction or diffusion terms.

3.2 Depth-Averaged MPM formulation

Following the works [22, 23, 14], we employ a semi-conservative variant of the Material Point Method (MPM) tailored to depth-averaged models. The MPM, initially developed as an extension of the Particle In Cell (PIC) method [49, 50], has recently gained significant attention due to its suitability for acceleration on modern parallel computing platforms [51, 52].

To adapt the MPM framework for the system of equations (1), it is essential to reformulate the left-hand side of the momentum equations by explicitly evaluating the spatial derivatives of the transport flux. For clarity, we restrict our focus to the x-momentum equation.

$$
u\partial_t(h) + h\partial_t(u) + u\partial_x(hu) + hu\partial_x(u) + \partial_x\left(\frac{1}{2}gh^2\right) + u\partial_y(hv) + hv\partial_y(u) = R.H.S. \tag{21}
$$

By using the continuity equation in (1), we replace the term $\partial_t(h)$, obtaining, after a few simplifications,

$$
h\,\partial_t(u) + hu\,\partial_x(u) + hv\,\partial_y(u) + \partial_x\left(\frac{1}{2}gh^2\right) = R.H.S. \tag{22}
$$

Note that we have left the pressure term $\partial_x(\frac{1}{2}gh^2)$ in the conservative form.

Now, since $\mathbf{v} = [u, v]^T$ and

$$
\frac{\mathrm{d}u}{\mathrm{d}t} = \partial_t(u) + \mathbf{v} \cdot \nabla u = \partial_t(u) + u\,\partial_x(u) + v\,\partial_y(u), \tag{23}
$$

collecting the term h in (22) and moving the pressure term $\partial_x(\frac{1}{2}gh^2)$ at the right-hand-side, we reach the form

$$
h\,\frac{\mathrm{d}u}{\mathrm{d}t} = \frac{1}{\rho}\,B_x + \frac{1}{\rho}\,\partial_x\left(\sigma_{xx}h - \frac{1}{2}\rho g h^2\right) + \frac{1}{\rho}\partial_y(\sigma_{xy}h) - gh\partial_x Z. \tag{24}
$$

Thus, the x-momentum equation is reformulated in terms of the material acceleration $\frac{\mathrm{d}u}{\mathrm{d}t}$. Next, all terms are multiplied by the density ρ, and the x-component of the pressure gradient, $\partial_x\left(\frac{1}{2}\rho g h^2\right)$, is combined with the x-component of the stress tensor term, $\partial_x\left(\sigma_{xx}h\right)$, ensuring that:

$$
\rho h\,\frac{\mathrm{d}u}{\mathrm{d}t} = B_x + \partial_x\left(\left[\sigma_{xx} - \frac{1}{2}\rho g h\right]h\right) + \partial_y(\sigma_{xy}h) - \rho g h\partial_x Z. \tag{25}
$$

The whole procedure can be applied to the y momentum in a similar fashion.

We now can define an effective stress tensor $\boldsymbol{\sigma}^{\nabla}$ that takes into account the hydrostatic pressure gradient simply as

$$\boldsymbol{\sigma}^{\nabla} = \boldsymbol{\sigma} - \frac{1}{2}\rho g h \otimes \mathbb{1}, \tag{26}$$

where $\boldsymbol{\sigma}$ is the Cauchy stress tensor defined in (3) and $\mathbb{1}$ is the identity tensor.

Finally, by setting $\mathbf{b} = -g\nabla Z$ we obtain a compact form that reads

$$\rho h \frac{\mathrm{d}\mathbf{v}}{\mathrm{d}t} = \mathbf{B}^f + \nabla \cdot (\boldsymbol{\sigma}^{\nabla} h) + \rho \mathbf{b} h, \tag{27}$$

and hence apply the MPM framework, according to [22, 23, 49, 50].

3.2.1 The DAMPM scheme

The initial stage involves examining the weak formulation of the momentum equations delineated in system (26). To accomplish this, we employ the Galerkin method, multiplying the equation by a suitably smooth test function ϕ and subsequently integrating it across the domain Ω. Ultimately, through the application of Green Theorem, we arrive at

$$\int_\Omega \rho h \frac{\mathrm{d}\mathbf{v}}{\mathrm{d}t}\,\phi\,d\mathbf{x} = \int_\Omega (\mathbf{B}^f + \rho \mathbf{b} h)\,\phi\,d\mathbf{x} - \int_\Omega \boldsymbol{\sigma}^{\nabla} h\,\nabla\phi\,d\mathbf{x} + \int_{\partial\Omega} \boldsymbol{\sigma}^{\nabla} h\,\phi\,\mathbf{n}\,d\mathbf{s}. \tag{28}$$

Here, $\mathbf{n}$ represents the outward unit normal to the boundary $\partial\Omega$. Concerning the boundary conditions of (28), we enforce a zero diffusive interface flux.

To discretize (28) we consider the material of interest composed by a finite collection Ω_p of N_p Lagrangian material points, which represent in this context columns of material. Each particle is provided with a mass m_p, which will be kept fixed throughout the simulations, and with the initial conditions on every physical quantity necessary to the constitutive model, such as velocities $\mathbf{v}_p = [u_p, v_p]^T$, locations $\mathbf{x}_p = [x_p, y_p]^T$, volumes V_p, areas A_p and stresses $\boldsymbol{\sigma}_p$, for all $p \in \{1, ..., N_p\}$. Following the standard MPM procedure [49, 22, 8], the mass m_p is concentrated on each columns as

$$\rho h(\mathbf{x}, t) = \sum_{p=1}^{N_p} m_p \delta(\mathbf{x} - \mathbf{x}_p),\ \forall \mathbf{x} \in \Omega,\ \forall t > 0, \tag{29}$$

where $\delta(\mathbf{x} - \mathbf{x}_p)$ is the Dirac delta function. By diving (29) by ρ, which is assumed constant, and by referring (28) with respect to (29) itself, we obtain

$$\sum_{p=1}^{N_p} m_p \frac{\mathrm{d}\mathbf{v}_p}{\mathrm{d}t}\phi_p = \sum_{p=1}^{N_p} A_p \mathbf{B}_p^f\,\phi_p + \sum_{p=1}^{N_p} \rho V_p\,\mathbf{b}_p\,\phi_p - \sum_{p=1}^{N_p} V_p \boldsymbol{\sigma}_p^{\nabla}\,\nabla\phi_p, \tag{30}$$

where A_p is the area of the column associated with the p^{th} particle, $\phi_p := \phi(\mathbf{x}_p)$ and $V_p = m_p/\rho$.

To calculate the differential terms in (30), we create a stationary Eulerian grid that spans the entire physical domain Ω of interest. This grid can take the form of either Cartesian or unstructured grids, with commonly employed element shapes including squares or triangles [8]. In the context of a comparison between the TG2 and DAMPM scheme, we consider in this work the same space $\mathbb{Q}^1$ of the piecewise bilinear polynomials as made as for the TG2 scheme, by covering the entire domain Ω with square elements, as shown in panel (a) of Figure 1.

Under these hyphoteses, we apply the standard finite element procedure on equation (30), obtaining

$$\sum_{i=1}^{N_v} \phi_i \cdot \sum_{j=1}^{N_v} M_{ij}\,\mathbf{a}_j = \sum_{i=1}^{N_v} \phi_i \cdot \sum_{p=1}^{N_p} A_p \mathbf{B}_p^f\,N_i(\mathbf{x}_p) + \sum_{i=1}^{N_v} \phi_i \cdot \sum_{p=1}^{N_p} \rho V_p\,\mathbf{b}_p\,N_i(\mathbf{x}_p) - \sum_{i=1}^{N_v} \phi_i \cdot \sum_{p=1}^{N_p} V_p\,\boldsymbol{\sigma}_p^{\nabla}\,\nabla N_i(\mathbf{x}_p), \tag{31}$$

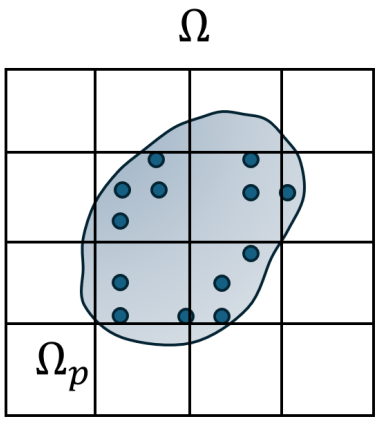

(a) A structured Eulerian grid is defined over the domain Ω, while the continuum material is discretized into a set Ω_p of N_p Lagrangian particles, each carrying its specific physical properties.

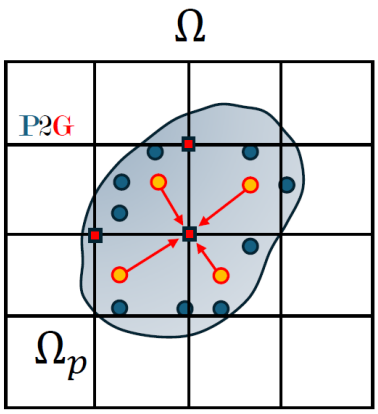

(b) Particle-to-Grid (P2G) Procedure: the physical quantities associated with the particles are projected onto the corresponding grid nodes using the basis functions $N_i(\mathbf{x}_p)$. This process is employed to compute and assemble the nodal forces $\mathbf{f}_i$.

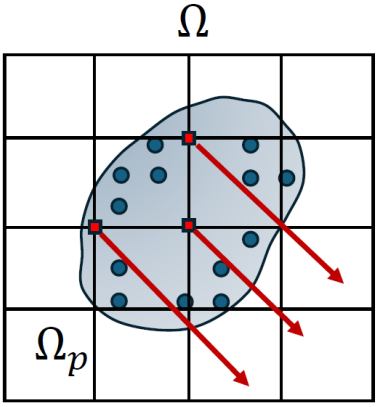

(c) Advective Phase on Grid Nodes: nodal accelerations $\mathbf{a}_i$ and velocities $\mathbf{v}_i$, illustrated with red arrows, are determined using the nodal momenta $(m\mathbf{v})_i$ and the total nodal force $\mathbf{f}_i$.

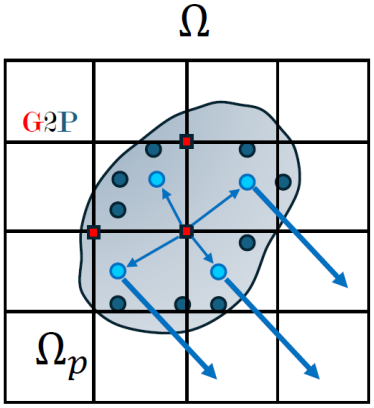

(d) The G2P procedure. The advective phase is projected back to the particles.

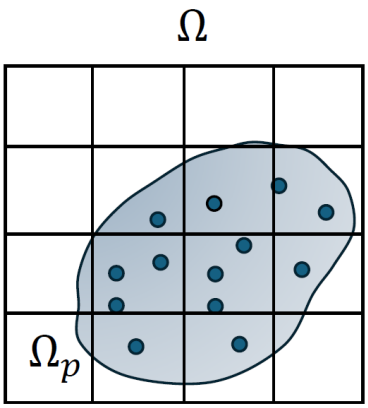

(e) Final stage of the method: once the particle stresses $\boldsymbol{\sigma}_p^{\nabla}$ are calculated, the particle positions $\mathbf{x}_p$ and their depths h_p are updated. This completes one iteration of the scheme, allowing the method to restart.

Figure 1: Illustration of the classic MPM algorithm.

.

which becomes

$$\sum_{j=1}^{N_v} M_{ij}\mathbf{a}_j \;= \sum_{p=1}^{N_p} A_p \mathbf{B}_p^f \, N_i(\mathbf{x}_p) + \sum_{p=1}^{N_p} \rho V_p \mathbf{b}_p \, N_i(\mathbf{x}_p) - \sum_{p=1}^{N_p} V_p \, \boldsymbol{\sigma}_p^{\nabla} \, \nabla N_i(\mathbf{x}_p), \quad \forall i \in \{1, ..., N_v\}, \tag{32}$$

since (31) is true for every sequence $\{\phi_i\}_{i\in\{1,\dots,N_v\}}$. Here, $N_i^1 := \phi_i^{(1)}$ are the same $\mathbb{Q}^1$ shape functions introduced in section 3.1 evaluated on $\mathbf{x}_p$ and M_{ij} is the mass matrix defined by

$$M_{ij} = \sum_{p=1}^{N_p} m_p \, N_i(\mathbf{x}_p) \, N_j(\mathbf{x}_p). \tag{33}$$

With the formulation shown in (32) we are able to apply the second stage of the MPM algorithm, which is the so called Particle-to-Grid (P2G) phase, as shown in panel (b) of Figure 1. We use the basis function N_i^1 to project the particle momenta $(m\mathbf{v})_p$ and to collect stresses $\boldsymbol{\sigma}_p^{\nabla}$, friction $\mathbf{B}_p^f$ and

body forces $\mathbf{b}_p$ on the ith grid nodes as

$$
\begin{aligned}
(m\mathbf{v})_i &= \sum_{p=1}^{N_p} (m\mathbf{v})_p N_i(\mathbf{x}_p), \\
\mathbf{f}_i^{\text{ext}} &= \sum_{p=1}^{N_p} \rho V_p \, \mathbf{b}_p N_i(\mathbf{x}_p), \\
\mathbf{f}_i^{\text{int}} &= \sum_{p=1}^{N_p} A_p \mathbf{B}_p^f \, N_i(\mathbf{x}_p) - \sum_{p=1}^{N_p} V_p \, \boldsymbol{\sigma}_p^{\nabla} \nabla N_i(\mathbf{x}_p),
\end{aligned}
\tag{34}
$$

where $\mathbf{f}_i^{\text{ext}}$ and $\mathbf{f}_i^{\text{int}}$ are intended as external and internal forces respectively. By using the lumped mass matrix M_i and by defining the total nodal forces $\mathbf{f}_i$ as the sum of $\mathbf{f}_i^{\text{ext}}$ and $\mathbf{f}_i^{\text{int}}$ we obtain, for every $i \in \{1, ..., N_v\}$ the final expression of (32) as

$$
M_i \mathbf{a}_i = \mathbf{f}_i. \tag{35}
$$

The third stage of the MPM framework, depicted in panel (c) of Figure 1, deals with the advective phase, in which the nodal forces $\mathbf{f}_i$ and momenta $(m\mathbf{v})_i$ are used to computed the nodal accelerations $\mathbf{a}_i$ and velocities $\mathbf{v}_i$, respectively as

$$
\mathbf{a}_i = \frac{\mathbf{f}_i}{M_i}, \qquad \mathbf{v}_i = \frac{(m\mathbf{v})_i}{M_i}. \tag{36}
$$

The use of an explicit time integration scheme allows us to compute the new nodal velocities at t^{k+1}, by setting

$$
\mathbf{v}_i^{k+1} = \mathbf{v}_i^k + \Delta t \, \mathbf{a}_i^k, \tag{37}
$$

where $\mathbf{v}_i^k$ and $\mathbf{a}_i^k$ are the velocities and accelerations computed with (36) at time t^k.

Once the advective phase is completed, the fourth stage of the algorithm can be performed as shown in panel (d) of Figure 1. In the Grid-to-Particle (G2P) process, the nodal velocities $\mathbf{v}_i^{k+1}$ just computed are projected back to the particles by using the shape functions N_i^1 as

$$
\mathbf{v}_p^{k+1} = \sum_{i=1}^{N_v} \mathbf{v}_i^{k+1} N_i^1(\mathbf{x}_p). \tag{38}
$$

The particle positions $\mathbf{x}_p^k$ can be updated by using the equation of the motion as

$$
\mathbf{x}_p^{k+1} = \mathbf{x}_p^k + \Delta t \, \mathbf{v}_p^k. \tag{39}
$$

In the last stage of the framework, depicted in panel (e) of Figure 1, we determine the updated particle stresses $\boldsymbol{\sigma}_p^{\nabla,\,k+1}$ employing the Update Stresses Last (USL) method [8, 9] and the depth h_p^{k+1}. In this way the stresses, based on the chosen constitutive model, are updated only after computing the nodal velocities $\mathbf{v}_i^{k+1}$. Thus, we must evaluate the strain increment $\Delta\varepsilon_p$ through the grid velocities $\mathbf{v}_i^{k+1}$ obtained from (37) as

$$
\Delta\varepsilon_p = \frac{\Delta t}{2} \sum_{i=1}^{N_v} \left(\nabla N_i(\mathbf{x}_p) \, \mathbf{v}_i^{k+1} + (\nabla N_i(\mathbf{x}_p) \, \mathbf{v}_i^{k+1})^T \right). \tag{40}
$$

Finally, we estimate the stress increment $\Delta\boldsymbol{\sigma}_p^{\nabla}$, by following the constitutive model shown in Section 2, as

$$
\boldsymbol{\sigma}_p^{\nabla,\,k+1} = \boldsymbol{\sigma}_p^{\nabla,\,k} + \Delta\boldsymbol{\sigma}_p^{\nabla}. \tag{41}
$$

We point out that, while the USL approach has demonstrated a tendency towards dissipation, its benefits in terms of stability and convergence outweigh those of other stress update techniques [53, 54].

The final stage of the method involves updating the depth h_p^{k+1} while ensuring the mass balance defined in (1). According to [22, 23, 14], the updated value of h_p^{k+1} is determined by

$$
h_p^{k+1} = \frac{h_p^k}{1 + \text{tr}(\Delta\varepsilon_p)}. \tag{42}
$$

4 Numerical simulations

In this section, we focus on the numerical comparison of the two schemes described in section 3 through accuracy and well-balancing tests. Before starting, we point out that the TG2 scheme is adaptive in space and allows for accurate tracking of the interface, whereas the DAMPM scheme does not. However, the Lagrangian nature of the particle-based method allows an accurate natural tracking of the wet interface, with the additional advantage of automatic mass balance preservation. We perform also a well-balancing test on a non-flat orography and, at the end of the section, we analyze a real case study consisting in a debris flow occurred at Rochefort Torrent, near Courmayeur (Aosta Valley, Italy) in September 2015.

4.1 Reliability test: dam break problem

The first test we carry out deals with a classic dam break problem on a frictionless domain $\Omega := [0, 300] \times [0, 20]$ described by the planar topography $Z(\mathbf{x}) = 100 - x/3$. We set a final time equal to 11s. Non-reflective boundary conditions are enforced on $\partial\Omega$, while we start from material at rest with the following initial material profile

$$h(\mathbf{x}, 0) = \begin{cases} 100 - Z(\mathbf{x}) & \text{if } x \leq 20, \\ 0 & \text{otherwise,} \end{cases} \tag{43}$$

and null velocities in both x and y directions.

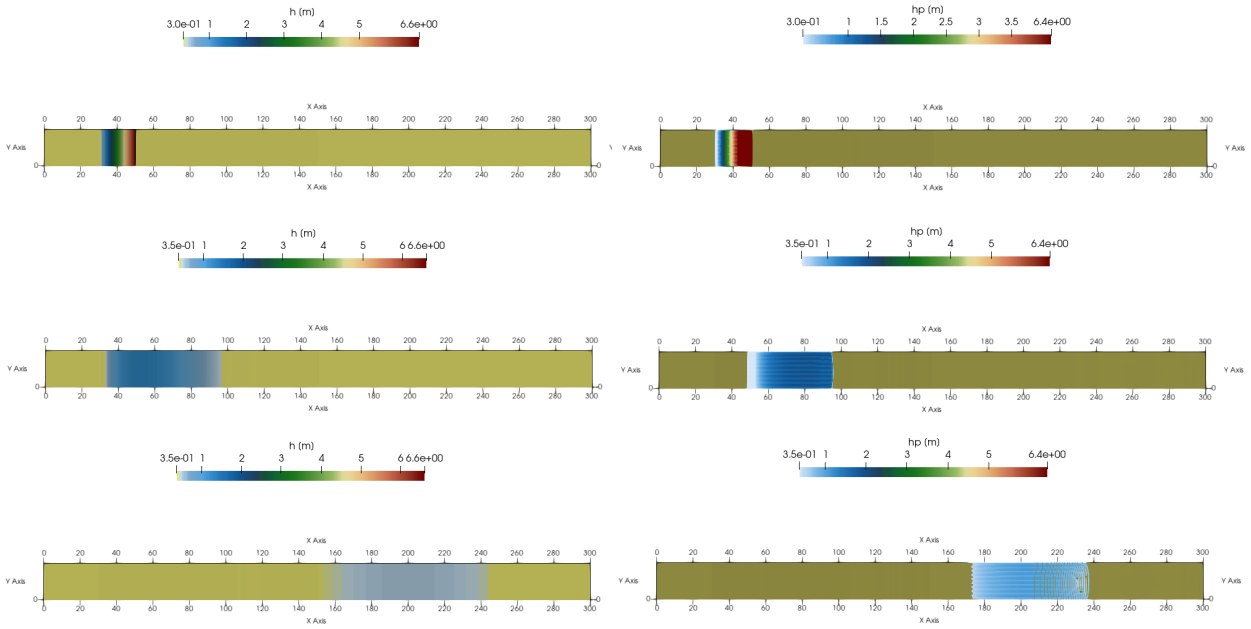

Figure 2: Inclined dam-break simulation. The left column represents the split IMEX-TG2-PC, while the right column shows the DAMPM simulation, both for the time instants $T = 0\ s$, $T = 5.5\ s$ and $T = 11\ s$

The water is free to collapse and flow under its own weight, and its motion is influenced solely by gravity along the inclined direction. We carried out the test by using both DAMPM and the IMEX-TG2-PC method.

The domain Ω has been discretized with $1.1 \cdot 10^4$ elements for the IMEX-TG2-PC. Regarding the DAMPM, we used the same spatial resolution, while we employed $7 \cdot 10^3$ particles to discretize the mass of water.

Despite the fundamentally different nature of the two approaches (particle-based for DAMPM and grid-based for IMEX-TG2-PC), both show similar behavior regarding the water front propagation.

However, it is observed that the DAMPM tends to be slightly more dissipative compared to the IMEX-TG2-PC, which is reflected in a difference in the velocities and final positions of the water front.

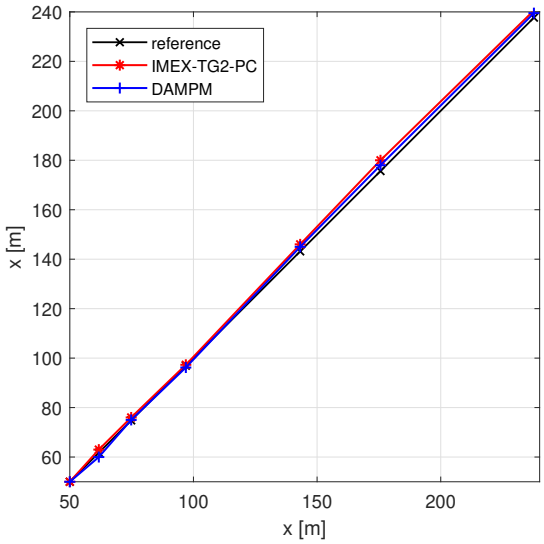

Figure 3: Parity plot for the inclined dam-break problem at different time instances. The positions shown correspond to the computed advancing front positions, compared with the expected positions for uniformly accelerated motion at the given time steps.

In Figure 2, three key time instants from the simulation are shown: $T = 0\ s$, $T = 5.5\ s$, and $T = 11\ s$. Starting from the same initial conditions, the water front in the Modified TG2 case is located at $x = 97.3\ m$ at time $T = 5.5\ s$, while in the DAMPM case, it is slightly further back at $x = 96.2\ s$, and at time $T = 11\ s$, the IMEX-TG2-PC reports the front at position $x = 240.6\ m$, compared to $x = 239.2m$ in the DAMPM method. This difference aligns with the observation that the particle-based method experiences greater numerical dissipation, leading to reduced front propagation over time.

Relative error generated on the front position		
Method	$T = 5.5\ s$	$T = 11\ s$
IMEX-TG2-PC	0.0039	0.0121
DAMPM	0.0074	0.0054

Table 1: Relative errors for the wet/dry inclined dam-break problem.

We compared the computed positions with the expected estimates, considering that a body descending a frictionless inclined plane follows a path of uniformly accelerated motion. The errors associated with the test are computed by comparing the two solutions with the exact one at the nodes of the computational grid. Table 1 demonstrates that both methods provide a good approximation of the theoretical behavior, while also highlighting the aforementioned differences in the treatment of numerical dissipation.

As a complementary analysis, Figure 3 presents the parity plot of the positions obtained from simulations using both methods, computed on the nodes of their respective grids, against the exact positions over the entire 11-second duration of the dam-break event. The analysis is based on sampled time instances $T = \{0, 2.75, 4, 5.5, 7.75, 9, 11\}\ s$, ensuring a representative distribution over the evolution of the event. This visualization reinforces that both methods yield results consistent with theoretical expectations, though slight discrepancies are observed. These deviations are primarily attributed to the distinct discretization strategies adopted for the momentum equations and the dissipation inherent in the DAMPM approach.

4.1.1 Collapse of a semisphere

The last test deals with the collapse of a semisphere of water under the action of gravity g on a flat, frictionless domain Ω described by the square $[0, 50]^2$. By the defining $\mathbf{x}_c = (25, 25)$, the initial conditions on the material read

$$\begin{aligned} h(\mathbf{x}, 0) &= \sqrt{25 - \|\mathbf{x} - \mathbf{x}_c\|^2} \\ u(\mathbf{x}, 0) &= v(\mathbf{x}, 0) = 0 \end{aligned} \qquad \mathbf{x} \in \Omega. \tag{44}$$

The total simulation time is set to $T = 1.2\,s$ and non-reflective boundary conditions are enforced at $\partial\Omega$. During the simulation of the collapse of the hemisphere, the debris front is allowed to expand

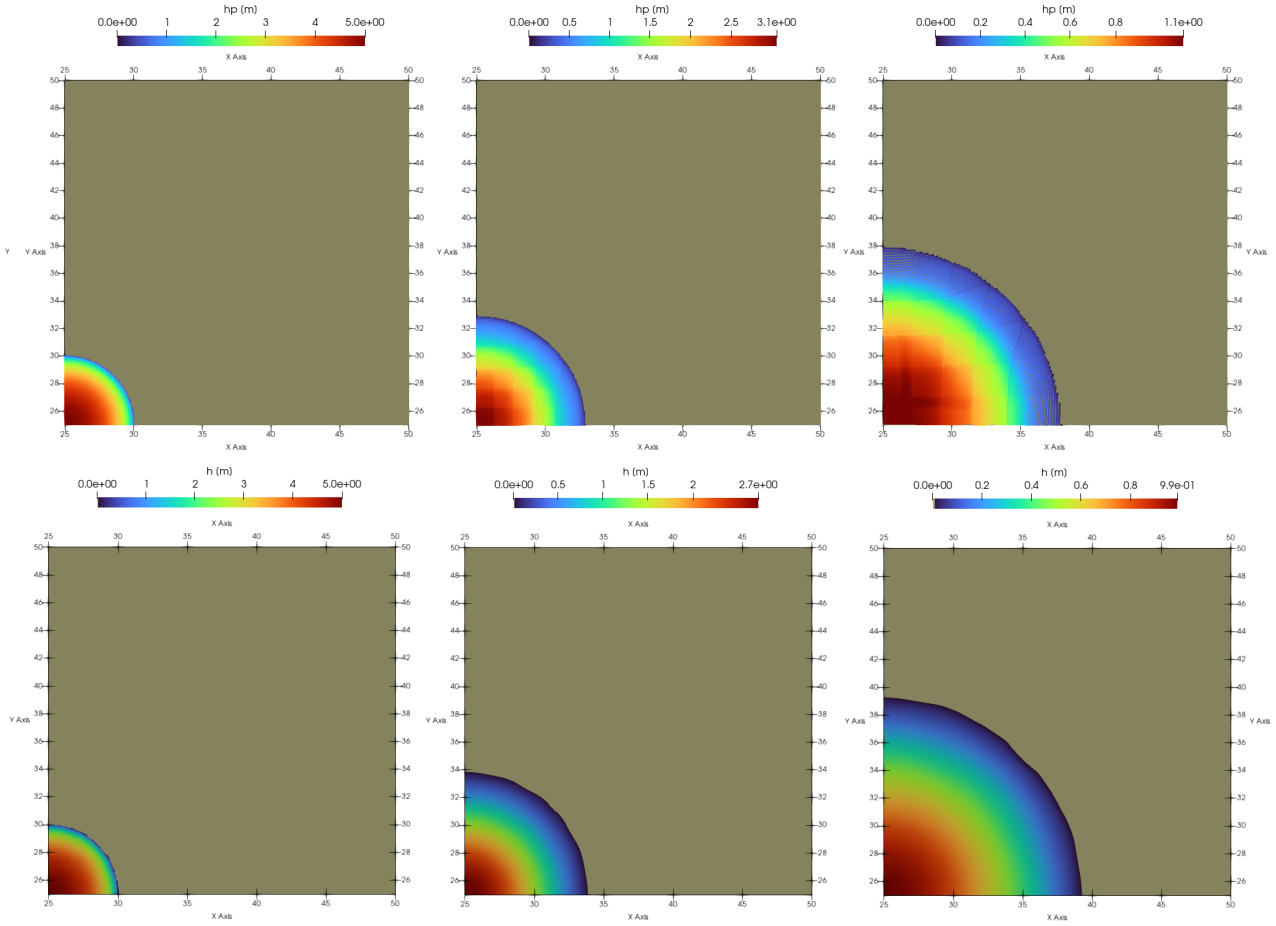

Figure 4: Snapshots of the sphere collapse for three different time instants $T = 0\,s$, $T = 0.6\,s$ and $T = 1.2\,s$ obtained with DAMPM (on the top) and TG2 (on the bottom), shown on the top-right quarter of the computational domain.

freely under the sole influence of hydrodynamic forces, moving across a flat, frictionless domain. This setup eliminates the influence of surface irregularities and frictional resistance, enabling a clear analysis of the dynamic behavior of the collapsing mass. The results obtained with both numerical approaches are entirely consistent, as illustrated in Figure 4, which presents three different time steps from the simulation conducted with each method.

The evolution of the debris flow demonstrates a rapid expansion of the initial mass, which starts with a diameter of approximately 5 meters and grows to about 13 meters after 1.2 seconds of simulation. This significant increase in the extent of the mass highlights the ability of both methods to accurately capture the physical dynamics of the spreading process. The temporal snapshots in Figure 4 reveal a high degree of agreement between the two approaches, with negligible differences in the spatial distribution and shape of the flow front over time.

These results further confirm the robustness of both numerical methods in modeling highly dynamic free-surface flows, where the interplay of inertial and hydrodynamic forces dominates the be-

havior of the system. By providing consistent and physically realistic results, both methods prove effective in capturing the fundamental characteristics of the hemisphere collapse scenario.

4.2 Well-balancing test

In order to verify the so called *lake-at-rest* condition in the context of MPM scheme, we need to slightly modify the formulation of the momenta equations in (1), by referring them to the still water level H, a straight line orthogonal to the gravity direction representing the rest position of a fluid. Following the works in [17, 14, 55, 56] and the notation of Figure 5, we first notice that, in the steady condition, it holds

$$\nabla H = -\nabla Z. \tag{45}$$

Then, by replacing the term $-gh\,\nabla Z$ in the right-hand-side of equation (1) with (45) and by adding

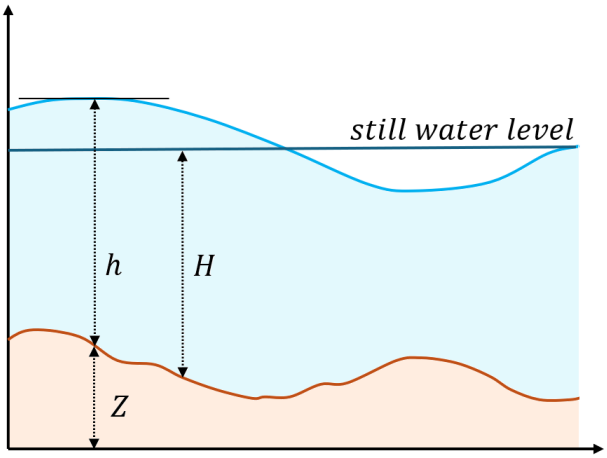

Figure 5: Lake-at-rest problem notation.

and subtracting the term $gH\,\nabla H$, after few simplifications we obtain a new, but equivalent, formulation of the system that reads

$$\partial_t(h\mathbf{v}) + \nabla\cdot\left(\mathbf{v}\otimes h\mathbf{v} + \frac{1}{2}g(h^2-H^2)\otimes\mathbb{1}\right) = \frac{1}{\rho}\mathbf{B}^f + \frac{1}{\rho}\nabla\cdot(h\boldsymbol{\sigma}) - g(h-H)\nabla Z. \tag{46}$$

We remark that the entire MPM framework can be still applied in an analogous fashion to the new formulation, which is, unfortunately, useful only as long as the still water level H is available.

Under these hypotheses, we have performed the well-balancing test by considering a topography Z described by the analytical equation

$$Z(\mathbf{x}) = 15\exp\left(-\|\mathbf{x}-\mathbf{x}_1\|^2\right) + 4\exp\left(-\|\mathbf{x}-\mathbf{x}_2\|^2\right) + 12\exp\left(-\|\mathbf{x}-\mathbf{x}_3\|^2\right), \quad \mathbf{x}\in\Omega=[0,10]^2, \tag{47}$$

where $\mathbf{x}_1 = [7/2, 7/2]^T$, $\mathbf{x}_2 = [7,7]^T$ and $\mathbf{x}_3 = [8, 5/2]^T$. We carried out the test by setting the initial conditions coinciding with the steady solutions, given by

$$\begin{aligned} &h(\mathbf{x},t) + Z_i(\mathbf{x}) = 10,\\ &u(\mathbf{x},t) = v(\mathbf{x},t) = 0, \end{aligned} \qquad \forall t\in(0,T],\ \mathbf{x}\in\Omega,\ i=1,2, \tag{48}$$

while setting the final time $T = 1\,s$ and $g = 9.81\,m/s^2$. The action of the bed friction $\mathbf{B}^f$ is taken into account by considering the Voellmy model defined in (2), with $\varphi = 26°$ and $\xi = 500\,m/s^2$. The Cauchy stress tensor $\boldsymbol{\sigma}$ has been defined following the Bingham model shown in (3), by setting $\rho = 1200\,kg/m^3$, $\mu = 2\cdot 10^3\,Pa$ and $\tau_Y = 30\,Pa\cdot s$. Finally, a null normal nodal velocity has been set at $\partial\Omega$.

	DAMPM		IMEX-TG2-PC	
State variable	$L^1(\Omega)$	$L^\infty(\Omega)$	$L^1(\Omega)$	$L^\infty(\Omega)$
h	$1.26e-12$	$1.26e-14$	$2.68e-13$	$8.92e-15$
hu	$1.08e-13$	$3.57e-14$	$2.38e-13$	$1.41e-14$
hv	$1.22e-13$	$3.25e-14$	$1.67e-13$	$2.02e-14$

Table 2: Well-balancing test results in $H^1(\Omega)$ and $L^\infty(\Omega)$ norms after $1\,s$ of simulation.

4.3 Real scenario

This section is devoted to the study of a real debris flow event occurred at Rochefort Torrent, highlighted in blue in Figure 6, situated in the Aosta Valley, northwest Italy. This basin lies within the Ferret Valley, nestled in the southeastern region of the Italian side of the Mont Blanc massif. Characterized by a glacial valley with a NE-SW orientation, it spans from the summit of Col Ferret ($2490\,m$ a.s.l) to the Entrèves municipality. Despite its relatively small basin area, numerous events have been documented, resulting in significant damage to local infrastructure, notably the Regional Road La Palud and its bridge over Rochefort Torrent, depicted in the bottom-right part of Figure 6 with a yellow cross.

In this study we focus on the analysis of the 2015 run-out event triggered by a brief yet intense rainfall, with cumulative precipitation exceeding $40\,mm$ over three days, peaking at around $9\,mm/h$ on the day of the event. Empirical surveys estimated approximately $6000\,m^3$ of deposition, highlighted in red in Figure 6, reaching a maximum thickness of about $1.5-2\,m$, in proximity of the bridge and along the road, while the complete event occurred in no more than few minutes.

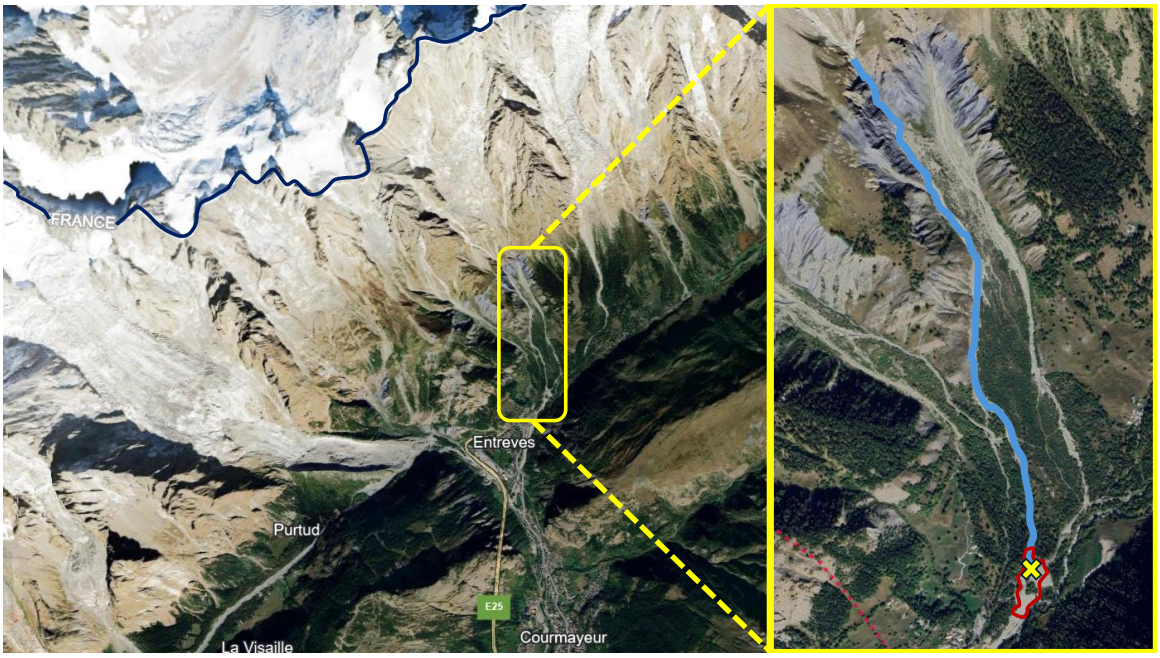

Figure 6: Location of the debris flow event with a magnification of the Rochefort Torrent, in blue, the bridge depicted with a yellow cross and the extension of the deposit, in red.

We carried out a simulation of the run-out phase of the debris flow with both numerical approaches, i.e. TG2 and DAMPM. Rheological parameters used in the Voellmy friction law are chosen by following the work of [57]. We considered only the action of the hydrostatic pressure gradient during the run-out and we set $\tan(\phi) \sim 0.15$ for friction angle, while we set a turbulence coefficient ξ equal to $500\,m/s^2$. The density ρ is fixed to $1750\,kg/m^3$ and it is chosen as an averaged of the span values who tipically refer such kind of phenomena [58]. Regarding the spatial discretization, a computational grid with $6.2 \cdot 10^4$ nodes was considered for both the IMEX-TG2-PC and DAMPM methods. The total number of particles used in the simulations was $3.1 \cdot 10^4$.

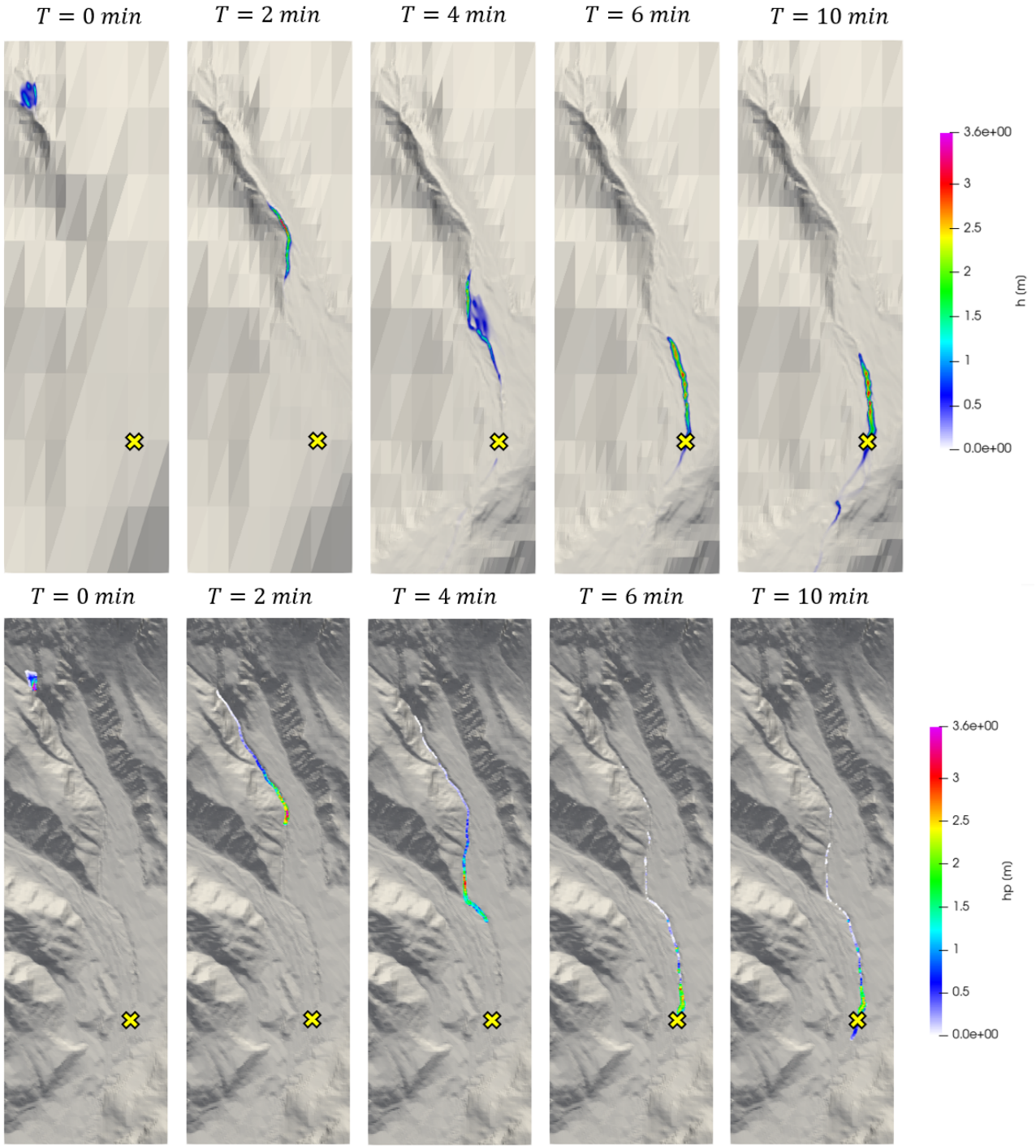

Figure 7: Snapshots of the Rochefort Torrent debris flow event with the split IMEX-TG2-PC and DAMPM for four different time instants, with respect to the bridge location, depicted with a yellow cross.

The test conducted on the debris flow in the Rochefort Torrent using the split IMEX-TG2-PC method and the DAMPM approach demonstrates results that are highly comparable and consistent with empirical observations. Both simulations were performed over a total time of 10 minutes, with an average time step Δt of approximately 0.06 s for both methods. Figure 7 presents various snapshots of the simulation with both methods at different time steps.

A key difference between the two approaches lies in their dissipative behavior. The DAMPM exhibits slightly more dissipative results compared to the split IMEX-TG2-PC method. This behavior has also been observed in previous numerical examples and is a characteristic of the DAMPM formulation. However, despite this dissipative tendency, the DAMPM proves to be exceptionally accurate

in describing the trajectory of the debris flow front, even in the highly complex topography under study. In contrast, the split IMEX-TG2-PC method provides a simulation where the debris flow front propagates slightly further, as seen in the central panel of Figure 7 at $T = 4\,min$.

Despite these differences, both methods produce a run-out prediction that aligns perfectly with empirical investigations. Both fronts reach the bridge downstream, marked with a yellow cross, in no more than 6 minutes after the initiation of the debris flow. This observation is corroborated by eyewitness accounts from individuals present during the event. Moreover, the average velocities calculated in the two simulations are consistent with the estimated flow velocity of the debris mass, which ranges between 3.0 and $3.5\,m/s$.

Figure 7 also illustrates that the average height of the deposited mass near the bridge does not exceed 2 m for either method. This result is entirely consistent with experimental observations and further confirms the accuracy of both approaches in modeling the event.

Finally, a comprehensive study of the efficiency and scalability of the two methods has not yet been reported, as the parallelization of the DAMPM approach is still under development. However, a comparison of computational times was conducted for the simulation of a realistic scenario, i.e., with a final time of $T = 10\,\text{min}$. The solvers were executed in serial mode on a machine equipped with an 8-core processor clocked at 1.70 GHz, using a similar spatial discretization of the computational domain.

The simulation performed with the IMEX-TG2-PC method, which is adaptive in both space and time, completed after approximately 16 hours, whereas the DAMPM simulation finished in 6 hours. The substantial difference in execution times is primarily attributed to the spatial adaptivity employed in the IMEX-TG2-PC method, as well as the front-tracking techniques, which impose smaller time-step sizes [6, 13].

On the other hand, another key advantage of the DAMPM approach is its accurate interface tracking capability, alongside its potential for parallelization on GPUs, enabling highly efficient and effective results [52, 59] .

5 Conclusions

In this study, we performed a qualitative comparative analysis of two numerical approaches: the split IMEX-TG2-PC method (mesh-based) and the Depth-averaged Material Point Method (particle-based). Both methods were fully derived, showcasing their theoretical underpinnings, and their accuracy and well-balancing properties were rigorously tested using well-established benchmarks from the literature. The results obtained are fully comparable and align with theoretical expectations, highlighting the robustness of both approaches.

In addition, the methods were applied to a real-world scenario involving a debris flow, with simulation outcomes validated against in situ observations. Both approaches demonstrated high accuracy in reproducing the run-out of landslides or debris flows, emphasizing their reliability in modeling complex natural phenomena. Notably, the DAMPM showed a slightly more dissipative behavior in its solutions, which may affect the precise quantification of energy dissipation, yet it proved particularly effective in capturing the dynamics of the advancing front over highly intricate topographies. Conversely, the IMEX-TG2-PC method maintained sharper resolution in areas where dissipation played a less dominant role but may encounter challenges in adapting to extremely irregular terrains.

Future work could focus on a detailed comparative analysis of computational efficiency and scalability, leveraging the power of GPUs to conduct simulations on larger domains and finer resolutions. This would provide a more comprehensive assessment of the strengths and limitations of these methods, enhancing their applicability to a broader range of real-world scenarios.

Data availability

Data will be made available from the corresponding author upon reasonable request.

Acknowledgements

This research was supported by the Accordo Attuativo ASI-POLIMI "Attività di Ricerca e Innovazione" n. 2018-5-HH.0.

C.d.F. and L.F. also acknowledge the support of "Dipartimento di Eccellenza 2023-2027".

Politecnico di Milano provided Open Access Funding within the CRUI-CARE agreement.

All authors are members of the Gruppo Nazionale Calcolo Scientifico-Istituto Nazionale di Alta Matematica (GNCS-INdAM).

Conflict of interest

The authors declare that they have no potential conflict of interest.

References

[1] U. Haque, P. F. Da Silva, G. Devoli, J. Pilz, B. Zhao, A. Khaloua, W. Wilopo, P. Andersen, P. Lu, J. Lee, et al., The human cost of global warming: Deadly landslides and their triggers (1995–2014), Science of the Total Environment 682 (2019) 673–684.

[2] U. Haque, P. Blum, P. F. Da Silva, P. Andersen, J. Pilz, S. R. Chalov, J.-P. Malet, M. J. Auflič, N. Andres, E. Poyiadji, et al., Fatal landslides in europe, Landslides 13 (6) (2016) 1545–1554.

[3] M. S. Bernardi, P. C. Africa, C. de Falco, L. Formaggia, A. Menafoglio, S. Vantini, On the use of interferometric synthetic aperture radar data for monitoring and forecasting natural hazards, Mathematical Geosciences 53 (8) (2021) 1781 – 1812.

[4] M. J. Froude, D. N. Petley, Global fatal landslide occurrence from 2004 to 2016, Natural Hazards and Earth System Sciences 18 (8) (2018) 2161–2181.

[5] M. Dilley, Natural disaster hotspots: a global risk analysis, Vol. 5, World Bank Publications, 2005.

[6] F. Gatti, M. Fois, C. de Falco, S. Perotto, L. Formaggia, Parallel simulations for fast-moving landslides: Space-time mesh adaptation and sharp tracking of the wetting front, Int J Numer Meth Fluids 95 (8) (2023) 1286–1309. doi:https://doi.org/10.1002/fld.5186.

[7] S. Idelsohn, E. Onate, To mesh or not to mesh. that is the question..., Comput. Methods Appl. Mech. Engrg. 195 (2006) 4681 – 4696.

[8] A. de Vaucorbeil, V. P. Nguyen, S. Sinaie, J. Y. Wu, Chapter two - material point method after 25 years: Theory, implementation, and applications, in: S. P. Bordas, D. S. Balint (Eds.), Advances in Applied Mechanics, Vol. 53 of Advances in Applied Mechanics, Elsevier, 2020, pp. 185–398. doi:https://doi.org/10.1016/bs.aams.2019.11.001.

[9] S. Bardenhagen, E. Kober, The generalized interpolation material point method, CMES - Computer Modeling in Engineering and Sciences 5 (06 2004).

[10] A. Sadeghirad, R. M. Brannon, J. Burghardt, A convected particle domain interpolation technique to extend applicability of the material point method for problems involving massive deformations, International Journal for Numerical Methods in Engineering 86 (12) (2011) 1435–1456. arXiv:https://onlinelibrary.wiley.com/doi/pdf/10.1002/nme.3110, doi:https://doi.org/10.1002/nme.3110.

[11] F. Gatti, C. de Falco, S. Perotto, L. Formaggia, A scalable well-balanced numerical scheme for the simulation of fast landslides with efficient time stepping, Applied Mathematics and Computation 468 (2024) 128525. doi:https://doi.org/10.1016/j.amc.2023.128525.

[12] F. Gatti, C. de Falco, S. Perotto, L. Formaggia, M. Pastor, A scalable well-balanced numerical scheme for the modeling of two-phase shallow granular landslide consolidation, Journal of Computational Physics (2024) 112798doi:https://doi.org/10.1016/j.jcp.2024.112798.

[13] F. Gatti, C. de Falco, M. Fois, L. Formaggia, A Scalable Well-balanced Numerical Scheme for a Depth-integrated Lava Flow Model, Available at SSRN 4846681 (2024).

[14] M. Fois, C. de Falco, L. Formaggia, A semi-conservative depth-averaged material point method for fast flow-like landslides and mudflows, Communications in Nonlinear Science and Numerical Simulation 138 (2024) 108202.

[15] W. R. Waldrop, Computational hydraulics: Elements of the theory of free surface flows. mb abbott. pitman publishing, london, 1979, 325 pp. (1979).

[16] A. Franci, M. Cremonesi, U. Perego, G. Crosta, E. Oñate, 3D simulation of Vajont disaster. Part 1: Numerical formulation and validation, Engineering Geology 279 (2020) 105854.

[17] M. Quecedo, M. Pastor, M. I. Herreros, J. A. Fernández Merodo, Numerical modelling of the propagation of fast landslides using the finite element method, International Journal for Numerical Methods in Engineering 59 (6) (2004) 755–794. arXiv:https://onlinelibrary.wiley.com/doi/pdf/10.1002/nme.841, doi:https://doi.org/10.1002/nme.841.
URL https://onlinelibrary.wiley.com/doi/abs/10.1002/nme.841

[18] M. Pastor, T. Blanc, B. Haddad, V. Drempetic, M. Mories, P. Stickle, M. Mira, J. Merodo, Depth averaged models for fast landslide propagation: mathematical, rheological and numerical aspects, Archive of Computational Methods in Engineering 22 (2015) 67–104.

[19] M. Mckinnon, O. Hungr, S. McDougall, Dynamic analyses of canadian landslides, Proceedings of the Fourth Canadian Conference on GeoHazards: From Causes to Management (2008) 20–24.

[20] S. Beguería, M. Hees, M. Geertsema, Comparison of three landslide runout models on the turnoff creek rock avalanche, british columbia, in: Landslide Processes Conference: A tribute to Theo van Asch. Strasbourg, 6-7 February, CERG, 2009, pp. 243–247. doi:10.13140/2.1.4569.3767.

[21] R. Sosio, G. Crosta, J. Chen, O. Hungr, Runout prediction of rock avalanches in volcanic and glacial terrains, Landslide Science and Practice: Spatial Analysis and Modelling 3 (2013) 285–291. doi:10.1007/978-3-642-31310-3-38.

[22] K. Abe, K. Konagai, Numerical simulation for runout process of debris flow using depth-averaged material point method, Soils and Foundations 56 (5) (2016) 869–888, special Issue on the International Symposium on Geomechanics from Micro to Macro IS-Cambridge 2014. doi:https://doi.org/10.1016/j.sandf.2016.08.011.

[23] L. Guillet, L. Blatny, B. Trottet, D. Steffen, J. Gaume, A depth-averaged material point method for shallow landslides: Applications to snow slab avalanche release, Journal of Geophysical Research: Earth Surface 128 (8) (2023) e2023JF007092, e2023JF007092 2023JF007092. arXiv:https://agupubs.onlinelibrary.wiley.com/doi/pdf/10.1029/2023JF007092, doi:https://doi.org/10.1029/2023JF007092.
URL https://agupubs.onlinelibrary.wiley.com/doi/abs/10.1029/2023JF007092

[24] J. Qiu, M. Dumbser, C.-W. Shu, The discontinuous Galerkin method with Lax–Wendroff type time discretizations, Computer methods in applied mechanics and engineering 194 (42-44) (2005) 4528–4543.

[25] M. Pastor, M. Quecedo, J. Fernández Merodo, M. Herrores, E. Gonzalez, P. Mira, Modelling tailings dams and mine waste dumps failures, Geotechnique 52 (8) (2002) 579–591.

[26] D. Givoli, Non-reflecting boundary conditions, Journal of computational physics 94 (1) (1991) 1–29.

[27] O. C. Zienkiewicz, K. Morgan, K. Morgan, Finite elements and approximation, Courier Corporation, 2006.

[28] C. Parés, Numerical methods for nonconservative hyperbolic systems: a theoretical framework., SIAM Journal on Numerical Analysis 44 (1) (2006) 300–321.

[29] M. Castro, J. Gallardo, C. Parés, High order finite volume schemes based on reconstruction of states for solving hyperbolic systems with nonconservative products. applications to shallow-water systems, Mathematics of computation 75 (255) (2006) 1103–1134.

[30] M. J. Castro, P. G. LeFloch, M. L. Muñoz-Ruiz, C. Parés, Why many theories of shock waves are necessary: Convergence error in formally path-consistent schemes, Journal of Computational Physics 227 (17) (2008) 8107–8129.

[31] S. Rhebergen, O. Bokhove, J. J. van der Vegt, Discontinuous galerkin finite element methods for hyperbolic nonconservative partial differential equations, Journal of Computational Physics 227 (3) (2008) 1887–1922.

[32] R. Abgrall, S. Karni, A comment on the computation of non-conservative products, Journal of Computational Physics 229 (8) (2010) 2759–2763.

[33] M. Dumbser, E. F. Toro, A simple extension of the osher riemann solver to non-conservative hyperbolic systems, Journal of Scientific Computing 48 (1) (2011) 70–88.

[34] J. Peraire, A finite element method for convection dominated flows, Ph.D. thesis, University College of Swansea, Swansea (1986).

[35] S. T. Zalesak, Fully multidimensional flux-corrected transport algorithms for fluids, Journal of computational physics 31 (3) (1979) 335–362.

[36] J. P. Boris, D. L. Book, Flux-corrected transport. iii. minimal-error fct algorithms, Journal of Computational Physics 20 (4) (1976) 397–431.

[37] D. Kuzmin, M. Möller, S. Turek, High-resolution fem–fct schemes for multidimensional conservation laws, Computer Methods in Applied Mechanics and Engineering 193 (45-47) (2004) 4915–4946.

[38] Y. Xing, X. Zhang, C.-W. Shu, Positivity-preserving high order well-balanced discontinuous Galerkin methods for the shallow water equations, Advances in Water Resources 33 (12) (2010) 1476–1493.

[39] J. G. Verwer, W. Hundsdorfer, B. P. Sommeijer, Convergence properties of the Runge-Kutta-Chebyshev method, Numerische Mathematik 57 (1) (1990) 157–178.

[40] J. G. Verwer, Explicit Runge-Kutta methods for parabolic partial differential equations, Applied Numerical Mathematics 22 (1-3) (1996) 359–379.

[41] J. G. Verwer, B. P. Sommeijer, An Implicit-Explicit Runge-Kutta-Chebyshev Scheme for Diffusion-Reaction Equations, SIAM Journal on Scientific Computing 25 (5) (2004) 1824–1835.

[42] R. Bermejo, P. G. del Sastre, An implicit-explicit Runge-Kutta-Chebyshev finite element method for the nonlinear Lithium-ion battery equations, Applied Mathematics and Computation 361 (2019) 398–420.

[43] B. Wohlmuth, Variationally consistent discretization schemes and numerical algorithms for contact problems, Acta Numerica 20 (2011) 569–734.

[44] R. L. Berge, I. Berre, E. Keilegavlen, J. M. Nordbotten, B. Wohlmuth, Finite volume discretization for poroelastic media with fractures modeled by contact mechanics, International Journal for Numerical Methods in Engineering 121 (4) (2020) 644–663.

[45] L. Formaggia, F. Gatti, S. Zonca, An XFEM/DG approach for fluid-structure interaction problems with contact, Applications of Mathematics 66 (2) (2021) 183–211.

[46] G. Strang, On the construction and comparison of difference schemes, SIAM Journal on Numerical Analysis 5 (3) (1968) 506–517.

[47] G. I. Marchuk, Some application of splitting-up methods to the solution of mathematical physics problems, Aplikace Matematiky 13 (2) (1968) 103–132.

[48] M. Quecedo, M. Pastor, A reappraisal of taylor–galerkin algorithm for drying–wetting areas in shallow water computations, International Journal for Numerical Methods in Fluids 38 (6) (2002) 515–531. arXiv:https://onlinelibrary.wiley.com/doi/pdf/10.1002/fld.225, doi:https://doi.org/10.1002/fld.225.
URL https://onlinelibrary.wiley.com/doi/abs/10.1002/fld.225

[49] D. Sulsky, Z. Chen, H. Schreyer, A particle method for history-dependent materials, Computer Methods in Applied Mechanics and Engineering 118 (1993) 179–196.

[50] D. Sulsky, Erratum: Application of a particle-in-cell method to solid mechanics, Computer Physics Communications (1995).

[51] X. Wang, Y. Qiu, S. R. Slattery, Y. Fang, M. Li, S.-C. Zhu, Y. Zhu, M. Tang, D. Manocha, C. Jiang, A massively parallel and scalable multi-gpu material point method, ACM Trans. Graph. 39 (4) (aug 2020). doi:10.1145/3386569.3392442.
URL https://doi.org/10.1145/3386569.3392442

[52] P. Baioni, T. Benacchio, L. Capone, C. de Falco, Gpus based material point method for compressible flows, in: Particles, 2023.
URL https://www.scipedia.com/public/Baioni_et_al_2023a

[53] P. Wallstedt, J. Guilkey, An evaluation of explicit time integration schemes for use with the generalized interpolation material point method, Journal of Computational Physics 227 (2008) 9628–9642. doi:10.1016/j.jcp.2008.07.019.

[54] S. Bardenhagen, Energy conservation error in the material point method for solid mechanics, Journal of Computational Physics 180 (2002) 383–403. doi:10.1006/jcph.2002.7103.

[55] B. Rogers, M. Fujihara, A. G. L. Borthwick, Adaptive q-tree godunov-type scheme for shallow water equations, International Journal for Numerical Methods in Fluids 35 (3) (2001) 247–280.

[56] B. D. Rogers, A. G. Borthwick, P. H. Taylor, Mathematical balancing of flux gradient and source terms prior to using roe's approximate riemann solver, Journal of Computational Physics 192 (2) (2003) 422–451. doi:https://doi.org/10.1016/j.jcp.2003.07.020.

[57] F. Vagnon, L. Kurilla, A. Clusaz, M. Pirulli, G. Fubelli, Investigation and numerical simulation of debris flow events in rochefort basin (aosta valley—nw italian alps) combining detailed geomorphological analyses and modern technologies, Bulletin of Engineering Geology and the Environment 81:378 (2022) 1–19.

[58] K. Long, S. Zhang, F. Wei, K. Hu, Q. Zhang, Y. Luo, A hydrology-process based method for correlating debris flow density to rainfall parameters and its application on debris flow prediction, Journal of Hydrology 589 (2020) 125124. doi:https://doi.org/10.1016/j.jhydrol.2020.125124.

[59] P. J. Baioni, T. Benacchio, L. Capone, C. de Falco, Portable, massively parallel implementation of a material point method for compressible flows (2024). arXiv:2404.17057.
URL https://arxiv.org/abs/2404.17057

MOX Technical Reports, last issues

Dipartimento di Matematica
Politecnico di Milano, Via Bonardi 9 - 20133 Milano (Italy)

102/2024 Bucelli, M.
The lifex library version 2.0

101/2024 Bonetti, S.; Corti, M.
Unified discontinuous Galerkin analysis of a thermo/poro-viscoelasticity model

100/2024 Farenga, N.; Fresca, S.; Brivio, S.; Manzoni, A.
On latent dynamics learning in nonlinear reduced order modeling

99/2024 Ragni, A.; Masci, C.; Paganoni, A. M.
Analysis of Higher Education Dropouts Dynamics through Multilevel Functional Decomposition of Recurrent Events in Counting Processes

98/2024 Castiglione, C.; Arnone, E.; Bernardi, M.; Farcomeni, A.; Sangalli, L.M.
PDE-regularised spatial quantile regression

97/2024 Ferro, N.; Mezzadri, F.; Carbonaro, D.; Galligani, E.; Gallo, D.; Morbiducci, U.; Chiastra, C.; Perotto, S.
Designing novel vascular stents with enhanced mechanical behavior through topology optimization of existing devices

93/2024 Conti, P.; Kneifl, J.; Manzoni, A.; Frangi, A.; Fehr, J.; Brunton, S.L.; Kutz, J.N.
VENI, VINDy, VICI - a variational reduced-order modeling framework with uncertainty quantification

95/2024 Zacchei, F.; Rizzini, F.; Gattere, G.; Frangi, A.; Manzoni, A.
Neural networks based surrogate modeling for efficient uncertainty quantification and calibration of MEMS accelerometers

96/2024 Brivio, S.; Fresca, S.; Manzoni, A.
PTPI-DL-ROMs: Pre-trained physics-informed deep learning-based reduced order models for nonlinear parametrized PDEs

94/2024 Franco, N.R.; Fresca, S.; Tombari, F.; Manzoni, A.
Deep Learning-based surrogate models for parametrized PDEs: handling geometric variability through graph neural networks